Available online at www.sciencedirect.com
SCIENCE DIRECT®
Journal of Solid State Chemistry 174 (2003) 392–402
JOURNAL OF SOLID STATE CHEMISTRY
http://elsevier.com/locate/jssc

Phase transitions in the $SrSnO_3$–$SrFeO_3$ solid solutions: X-ray diffraction and Mössbauer studies

P. Schmid Beurmann,[a,*] V. Thangadurai,[b] and W. Weppner[b]

[a] *Institute for Geosciences, University of Kiel, Ohlshausenstr. 40, 24098 Kiel, Germany*
[b] *Chair for Sensors and Solid State Ionics, Faculty of Engineering, University of Kiel, Kaiserstr. 2, 24143 Kiel, Germany*

Received 28 January 2003; received in revised form 29 April 2003; accepted 7 May 2003

Abstract

$SrSn_{1-x}Fe_xO_y$ ($0 \leqslant x \leqslant 1$) oxides were prepared by conventional solid-state reaction in air using high-purity ($\geqslant 99\%$) $SrCO_3$, SnO_2 and $Fe(C_2O)_2 \cdot 2H_2O$ at elevated temperatures of 1300°C for 24 h and furnace cooled. Samples obtained from 1300°C were annealed at 620°C for 2 days and quenched in liquid nitrogen (LN). Powder XRD analysis by Rietveld refinement and Fe Mössbauer spectroscopy measurements were employed to characterize synthesized perovskites. Samples obtained from furnace cooled and LN quenched undergo two compositionally driven phase transitions, which are supposed to be of second order. The $x = 0$–0.3 members crystallize in orthorhombic parent $SrSnO_3$ structure (Space group *Pbnm*), whereas samples $x = 0.4$–0.9 have a simple cubic perovskite cell and end-member $SrFeO_{2.74}$ composition crystallize orthorhombic structure (Space group *Cmmm*). The composition of the first phase transition ($x \approx 0.3$) is slightly shifted to higher x with decreasing annealing temperature. Mössbauer data show that the Fe^{4+}/Fe^{tot} ratio is depending on composition under constant synthesis conditions. The phase compositions have been discussed in terms of ternary solid solution of compounds $SrSnO_3$–$SrFeO_{2.74}$–$SrFeO_{2.5}$ superior to a simple binary solid solution ($SrSnO_3$–$SrFeO_3$).

1. Introduction

In recent years, there has been a continuous interest to develop new materials with perovskite structure. Perovskites are generally transition metal oxides with general formula ABO_3 (A = mono or di or trivalent metal ions; B = tri or tetra or pentavalent metal ions). In the perovskite structure, the B-site cations occupy the interstitial site of an octahedron of oxygen anions, and corner-sharing BO_6 form the perovskite unit cell. The A-site cation fits in the large cavity at the center of 12 coordination site [1,2]. Goldschmidt's tolerance factor, $t = r_A + r_O/\sqrt{2}(r_B + r_O)$ (where r_A, r_B, r_O are empirical radii of respective ions), determine the size of the A-cation. The ideal cubic perovskite structure should have $t = 1$. The perovskite structure occurs within the range $0.75 < t < 1.00$ [2]. The nature and stoichiometry of the A and B-site cations, determine the physical properties, for example, ferroelectricity (e.g., $KNbO_3$, $BaTiO_3$), ferromagnetism (e.g., $La_{0.5}Sr_{0.5}MnO_3$, $SrRuO_3$), superconductivity (e.g., $YBa_2Cu_3O_7$), metallic conductivity (e.g., $La_{1-x}Sr_xCoO_3$) and ionic conductivity (e.g., $La_{1-x}Sr_xGa_yMg_yO_3$). The interesting electrical and magnetic properties are due to narrow electronic bands (1–2 eV) between the metal d and the oxygen p orbitals [3–5]. Furthermore, perovskite type materials have also drawn much attention recently due to existence of mixed ionic and electronic conduction, which finds application in many catalytic reactions and membrane for gas separations [4]. In perovskites, which contains transition metals, especially Mn, Co, Ru, Ni, Fe and Cr, the existence of mixed or intermediate valence states is critical for many of those properties [5].

The magnetic properties of the system $SrSnO_3$–$SrFeO_y$ were investigated recently [6] by powder XRD and Mössbauer spectroscopy and SQUID. $SrSn_{1-x}Fe_xO_y$ forms a non-stoichiometric solid solution between fully oxidized strontium stannate $SrSnO_3$ and oxygen deficient strontium ferrate $SrFeO_{2.73}$. The electronic conductivity increases with increasing x and decreasing activation energy [6]. However, our recent study shows that the compounds with low Fe content are mixed

*Corresponding author. Fax: +49-431-880-4457.
E-mail addresses: psb@min.uni-kiel.de (P.S. Beurmann), ww@tf.uni-kiel.de (W. Weppner).

0022-4596/03/$ - see front matter © 2003 Elsevier Inc. All rights reserved.
doi:10.1016/S0022-4596(03)00258-5

oxide ion and electronic conductor and high Fe content exhibits a predominant electronic conductor [7,8].

At room temperature the tin end-member $SrSnO_3$ crystallizes in orthorhombic space group *Pbnm* (SG No. 62) with all the tin ions being symmetrically identical [9]. Material quenched from high temperatures shows at first a simple cubic XRPD but after 1–2 h reflections of orthorhombic double cubic cell appear [10].

The Fe end member exhibits complex structural chemistry, which depends very much on the synthesis conditions such as temperature and atmosphere. For example, under ambient synthesis conditions, the composition of the slowly cooled sample in air was found to be $SrFeO_{2.80}$–$SrFeO_{2.85}$ [11]. Recently, it has been reported that non-stoichiometric $SrFeO_y$ has three modifications with different amounts of oxygen vacancy concentrations: cubic for $2.97 > y > 3.0$, tetragonal for $y = 2.875$ and orthorhombic for $y = 2.75$ [12]. Besides, recently, an orthorhombic structure for the nominal composition $SrFeO_{2.74}$ was reported [13], which crystallizes in an orthorhombic space group *Cmmm* (SG No. 65). In contrast to $SrSnO_3$, there are two different *B*-positions present in equal amounts: one is occupied by Fe^{4+} in octahedral coordination the other being Fe^{3+} in a tetragonal pyramidal site.

Roh et al. [6] reported cubic cell for all the members of $SrSn_{1-x}Fe_xO_3$ ($0 \leqslant x \leqslant 1$). In view of the complex structural chemistry of Fe-end member, we aimed to investigate in detail about the evolution of structure of solid solution $SrSnO_3$–$SrFeO_y$ under different synthesis conditions. Accordingly, the present paper shows the crystal chemical properties of the members of the $SrSn_{1-x}Fe_xO_y$ solid solutions that change with compositions and compositionally driven phase transitions appear between $x = 0.9$ and 1.

2. Experimental procedure

2.1. Synthesis

$SrSn_{1-x}Fe_xO_y$ ($0 \leqslant x \leqslant 1$) perovskite oxides were prepared in air by solid-state reaction of stoichiometric mixtures of $SrCO_3$ (99.9 + %—Aldrich), SnO_2 (99.9%—Alfa) and Fe $(CO_2)_2 \cdot 2H_2O$ (99%—Aldrich). Furnace cooled (FC) samples were synthesized at 1000°C and 1300°C for 24 h with intermittent grinding and pelletising using isostatic pressures [7]. After reaction furnace was switched off and the samples were cooled down to room temperature over night. A homogenized part of the material further denoted as "quenched samples" was additionally heated at 620°C for 48 h and then quenched in liquid nitrogen (LN) within seconds. According to Fournés et al. [23], such a procedure leads to a composition of $SrFeO_{2.75}$ in case of Fe end-member composition.

2.2. X-ray powder diffraction

Sintered pellets of the furnace cooled samples were cut into small coin shaped cylinders. A portion of the pellets was ground to fine powder for phase characterization. X-ray powder patterns were recorded using a SIEMENS D5000 powder diffractometer with Cu$K\alpha$ radiation and a secondary graphite (001) monochromator with the operation conditions $U = 40$ kV and $I = 30$ mA. Rietveld analysis was performed using the program HILL 8 [14].

2.3. ^{57}Fe-Mössbauer spectroscopy

Typical members of the solid solution were characterized by Mössbauer spectroscopy to identify the valence states of Fe in the $SrSn_{1-x}Fe_xO_y$ perovskites using a ~0.5 GBq ^{57}Co/Cr source at room temperature in combination with a constant-acceleration spectrometer. For absorber preparation about 40 mg of $Sr(Sn,Fe)O_y$ sample were diluted in 150 mg of avicel as a matrix and pressed to pellets with a diameter of 1/2 an inch. This procedure resulted in absorber densities between 6 and 10 mg Fe/cm^2. The isomer shifts were given relative to ^{57}Fe in α-Fe. All spectra were corrected for thickness effects [15]. The average recoilless fraction was estimated to have a value of $f = 0.75$. The spectra were analyzed using the MOSMOD program package [16] applying Voigtian line-shape to the absorption lines with a variable Gaussian QS-distribution parameter σ. The lorentzian line width of the incident γ-radiation was kept to natural value of 0.195 mm/s.

The oxygen stoichiometry of $SrFeO_y$ perovskite was already determined by several authors (e.g., by using titration methods or DTG [6,12,17,24]). Takeda et al. [12] found good agreement between chemical analysis and Mössbauer data for the oxygen stoichiometry of several $SrFeO_y$ samples. Fournés et al. [17] determined stoichiometry of $SrFeO_y$ ($y = 2.75$ at 620°C) in good agreement to our value of 2.74 determined by Mössbauer spectroscopy. Concerning Sn-containing samples Roh et al. [6] found that stoichiometry of $Sr(Sn_{1-x}Fe_x)O_y$ compounds calculated from Mössbauer area ratios are consistent with data from the chemical analysis for the compositions with $x = 0.75$ and $x = 1.00$. Therefore, we determined the oxygen stoichiometry using ^{57}Fe-Mössbauer spectroscopy.

3. Results

3.1. Optical characterization of the run products

The samples consisted of fine-grained crystals the diameters of which were determined to be less than 10 μm using optical microscopy on sample material

dispersed in ethanol. The color of the material changed with increasing content of $SrSnO_3$ component from black in case of the $SrFeO_y$ end-member to beige for pure $SrSnO_3$. No visible difference in color could be stated between furnace cooled and liquid N_2 quenched samples.

3.2. X-ray powder diffraction

The powder diffractions of the quenched and furnace cooled compounds are presented in Fig. 1. The patterns of samples with high tin content show additionally to the basis reflections of the simple cubic perovskite (*hkl*)-c several weak Bragg peaks, which reflect the orthorhombic distortion of the structure. Therefore, we refined the diffractograms of Sn-rich members using the lattice constants and structural data of $SrSnO_3$ as starting parameters [9]. Additionally, to the reflections of the $Sr(Sn,Fe)O_y$ phase the diffraction patterns show reflections at 28° (2θ) which are most probably due to unreacted starting material. E.g., $SrCO_3$ (JCPDS-ICDD

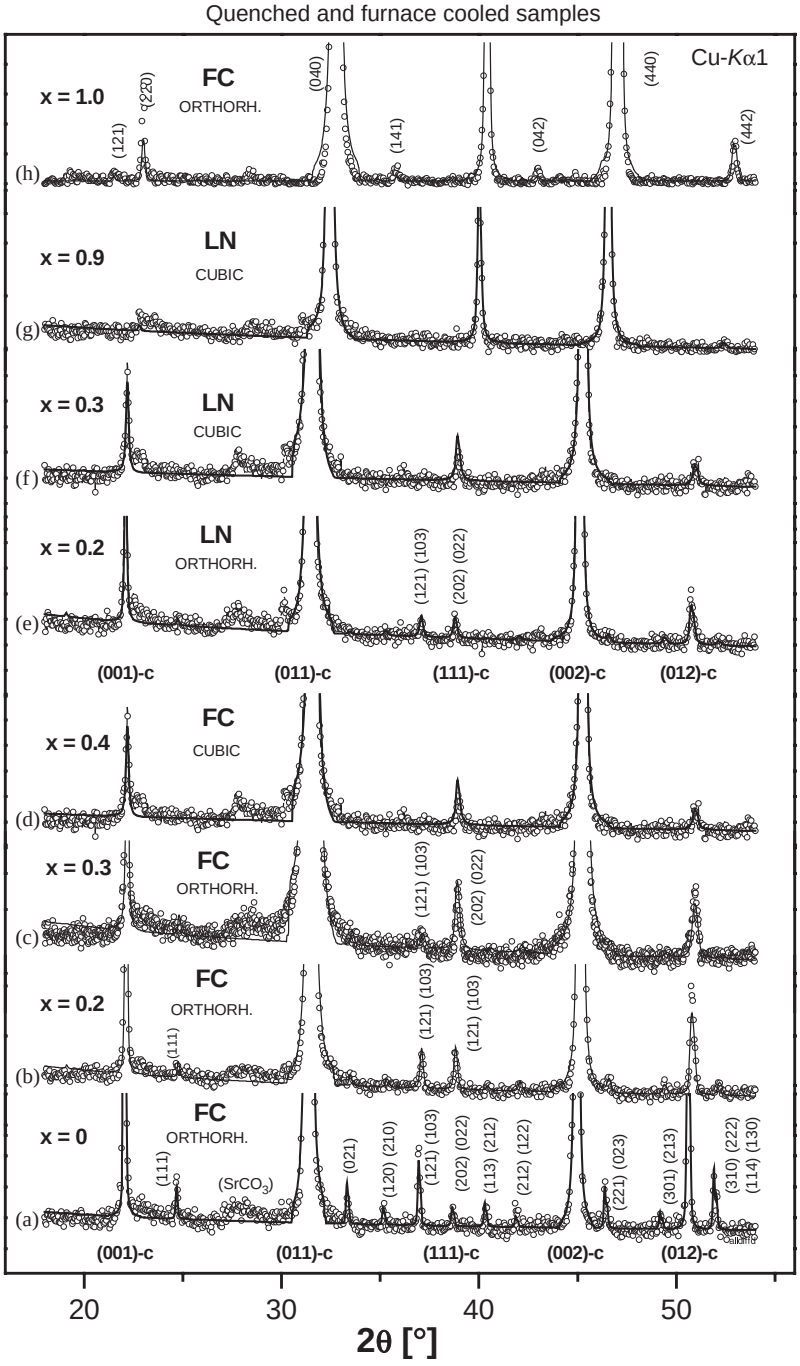

Fig. 1. XPRD of members of the $SrSn_{1-x}Fe_xO_y$ solid series quenched from 620°C (LN) and furnace cooled (FC) members. The phase transition from orthorhombic to cubic takes place between $x = 0.3$ and 0.4 for the FC and between $x = 0.2$ and 0.3 for the LN-samples.

Table 1
Lattice parameters of $SrSn_{1-x}Fe_xO_y$ perovskites at room temperature

Perovskite		Lattice parameters (Å)		
		a	*b*	*c*
$SrSnO_3$	FC	5.7082(3)	5.7035(3)	8.0659(6)
$SrSn_{0.9}Fe_{0.1}O_y$	LN	5.7015(7)	5.6914(7)	8.047(1)
	FC	5.6987(4)	5.6937(8)	8.0509(8)
$SrSn_{0.85}Fe_{0.15}O_y$	LN	5.699(1)	5.684(1)	8.036(2)
	FC	5.690(1)	5.685(1)	8.045(1)
$SrSn_{0.7}Fe_{0.3}O_y$	LN	4.0045(2)		
	FC	5.680(1)	5.659(1)	8.000(2)
$SrSn_{0.6}Fe_{0.4}O_y$	LN	3.9955(3)		
	FC	3.9934(2)		
$SrSn_{0.5}Fe_{0.5}O_y$	LN	3.9830(3)		
	FC	3.9788(2)		
$SrSn_{0.4}Fe_{0.6}O_y$	LN	3.9688(4)		
	FC	3.967(1)		
$SrSn_{0.3}Fe_{0.7}O_y$	LN	3.9492(5)		
	FC	3.9450(2)		
$SrSn_{0.1}Fe_{0.9}O$	LN	3.9009(3)		
	FC	3.8973(2)		
$SrFeO_y$	LN	10.9715(8)	7.7121(5)	5.4733(5)

Note: LN: samples quenched to liquid nitrogen from 620°C after 48 h; FC: furnace cooled samples.

77-1798) has its strongest reflection at 27.7°. As the intensity of the reflection at around 28° is about 0.2% of the most intense reflection of the $Sr(Sn,Fe)O_y$ phase the presence of such impurities do not disturb the chemical composition of our solid solutions significantly. With increasing Fe-content the superstructure reflections become continuously weaker. Above $x = 0.2$, they disappear in the LN samples and above $x = 0.3$ in the FC samples. The diffractograms of intermediate compositions up to $x = 0.9$ could be refined using the data of the simple cubic perovskite [2].

In the diffraction pattern of end-member $SrFeO_y$ again superstructure reflections appear which could be indexed on orthorhombic cell (see Table 1) and be refined using the structural data of $SrFeO_{2.74}$ [13].

Table 1 lists the lattice parameters of FC and LN samples and Table 2 the final atomic coordinates obtained from the XRD refinement for furnace cooled samples.

Fig. 2 shows the lattice parameters vs. composition of the quenched samples. In order to better present the variations with composition orthorhombic lattice parameters were transformed to pseudocubic perovskite cell. The data points of the furnace cooled samples are not shown because of complete overlap due to the small differences.

3.3. ^{57}Fe-Mössbauer spectroscopy

The measured and calculated Mössbauer spectra of four members of the solid solutions from both synthesis routes are given in Figs. 3 and 4. The evaluated Mössbauer parameters of the different species resulting from a fitting procedure are given in Tables 3 and 4.

Table 2
Furnace cooled samples: structural parameters of $Sr(Sn,Fe)O_y$ from the Rietveld refinement at room temperature in space group *Pbnm*. $Z = 4$

	$SrSnO_3$[24]	$SrSnO_3$	$x = 0.2$	$x = 0.3$
Sr	−0.0009	−0.006(3)	−0.004(5)	0.00(1)
x	0.0124	0.023(1)	0.014(1)	0.00(4)
y	1/4	1/4	1/4	1/4
z				
Sn/Fe	0	0	0	0
x	1/2	1/2	1/2	1/2
y	0	0	0	0
z				
O1	0.0736	0.05(2)	0.08(1)	0.04(3)
x	0.4896	0.495(6)	0.50(1)	0.42(2)
y	1/4	1/4	1/4	1/4
z				
O2	0.7132	0.712(7)	0.76(1)	0.76(4)
x	0.2853	0.25(1)	0.28(1)	0.27(4)
y	0.0368	0.033(8)	0.01(1)	0.01(2)
z				
$B_{overall}$		0.30(2)	0.60(1)	1.02(2)
R_p/R_{wp}		7.4/9.8	6.2/8.3	6.8/8.7
GOF/R_{exp}		1.3/5.6	1.3/4.9	1.6/4.4
R_{Bragg}		3.2	1.74	1.14

Note: Site occupancies for oxygen were set to unity. Those of the Sn/Fe position were calculated from the nominal composition.

3.3.1. LN quenched samples

The spectra (Figs. 3d–g) were fitted using Voigtian subspectra arbitrarily denoted as A, B, C and D. The spectrum of the end-member $SrFeO_y$ (Fig. 3g) is quite similar to those of Takeda et al. [12] and Fournés et al. [17] but differs significantly from that of Roh et al [6], as the latter shows a higher absorption between the high-velocity peaks of subspectra A and B. Subspectrum C was found to be necessary in order to fit the absorption between the high-velocity peaks of subspectra A and B. With increasing Sn-content (e.g., sample with $x = 0.9$ in Fig. 3) the line width of the subspectra increases rapidly lowering the resolution of the spectra. Therefore, it was sufficient to fit the spectrum of sample $x = 0.9$ using only two subspectra A and B. In the intermediate part of the system the main peaks become more similar in absorption and developed a shoulder on the left side of the low-velocity peak. This shoulder was used as a constraint for subspectrum D.

3.3.2. FC furnace cooled samples

The spectrum of iron end-member $SrFeO_y$ (Fig. 4a) corresponds well to sample with $y = 2.80$ of Takeda et al. [12] and was therefore treated as a two phase

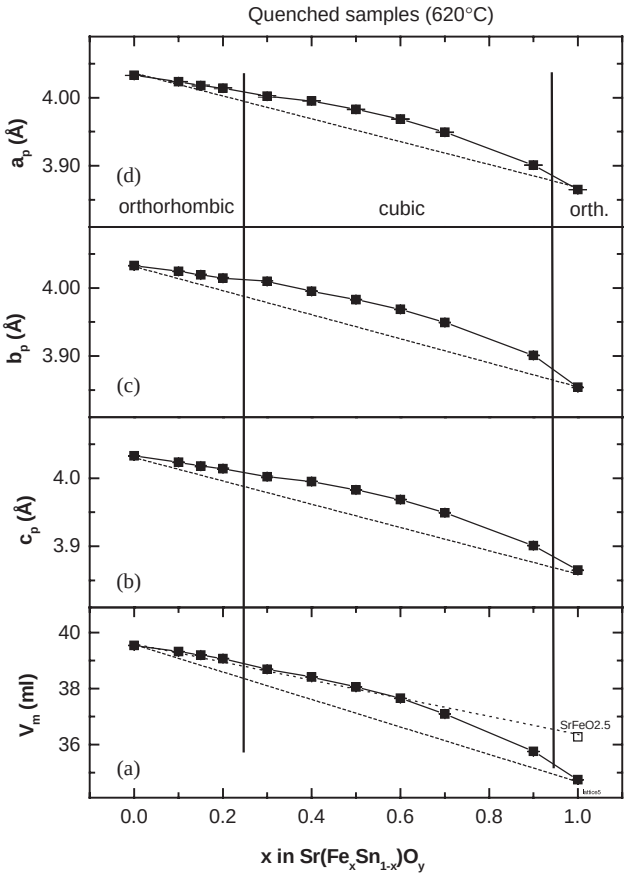

Fig. 2. Lattice constants and molar volume vs. composition of the $SrSn_{1-x}Fe_xO_y$ solid series (samples quenched from 620°C). The pseudocubic lattice constants of the orthorhombic phases were calculated according to the formula: $a_p^{orth} = a^{orth}/\sqrt{2}$, $b_p^{orth} = b^{orth}/\sqrt{2}$, $c_p^{orth} = c^{orth}/2$.

mixture of orthorhombic $SrFeO_{2.73}$ and tetragonal $SrFeO_{2.86}$ perovskite. The spectra of the solid solutions were fitted using three doublets denoted as A, B and E.

Which increasing Sn-content the line width of the subspectra become broader (Figs. 4b–d) as in the case of the quenched samples. But in contrast to the latter, the main peaks at around -0.1 and $+0.7$ mm/s do not become equal in intensity and do not develop a shoulder on the left side of the low-velocity absorption. This reveals substantial differences in abundance of the Fe-species in the products of the different syntheses routes.

3.3.3. Determination of compositional parameter y ($SrSn_{1-x}Fe_xO_y$)

The oxygen compositional parameter y according to the formula of $SrSn_{1-x}Fe_xO_y$ was determined using the area ratios of Mössbauer species (Tables 3 and 4) and additionally in case of Fe end-member samples using a calibration function (Fig. 5). The latter plot shows the molar volume of our Fe end-member samples of the system $SrFeO_y$ together with literature data. According to the linear regression function $V_m = 40.3(6) - 2.0(2)y$ (cm^3/mol) (Eq. (1)) our quenched and furnace cooled end-member samples have a composition of $y = 2.74$ and 2.80 in agreement to the Mössbauer results ($y = 2.74$ and 2.82, see Tables 3 and 4). Following the results of Takeda et al. [12] the quenched $SrFeO_{2.74}$ sample has a composition near orthorhombic perovskite with $y = 2.75$ whereas the furnace cooled sample is located within the miscibility gap between the $y = 2.75$ and 2.875 member.

4. Discussion

4.1. Compositional properties

The compositional relations are visualized in the ternary phase diagram $SrSnO_3$–$SrFeO_{2.5}$–$(1/4)O_2$ (Fig. 6) which shows the representing data points, calculated from Mössbauer data, of our samples together with those of Roh et al. [6]. In case of our quenched samples and those of [6] the Fe end-member has a composition of $SrFeO_{2.73(1)}$, whereas the furnace cooled sample has a composition of $SrFeO_{2.80}$ and is therefore located within the miscibility gap in the $SrFeO_y$ system. Solid solutions with increasing Sn content show an increasing deviation from the binary join $SrSnO_3$–$SrFeO_{2.73}$. Consequently, our investigated phases and also those of Roh et al. [6] are not members of simple binary solid solutions between $SrSnO_3$ and $SrFeO_{2.73}$. The latter would imply a constant Fe^{4+}/Fe^{tot} ratio but Mössbauer results show that the portion of Fe^{4+} with respect to the total iron content decreases with increasing Sn content (Fig. 7). Consequently, the composition of the $Sr(Sn,Fe)O_y$ solid solutions have to be described as to be composed of a $SrSnO_3$, a $SrFeO_{2.73}$ and a $SrFeO_{2.5}$ component. The curved line of representing data points in Fig. 6 cannot be explained by slow cooling in combination with a higher mobility of the oxygen ions in the iron rich phases because samples quenched from different temperatures and furnace cooled samples show the same trend.

According to Fig. 6 it is more appropriate to describe Sn-rich samples as solid solutions between $SrSnO_3$ and $SrFeO_{2.5}$ as their representing data points are located nearer to the $SrSnO_3$–$SrFeO_{2.5}$ binary join than to the $SrSnO_3$–$SrFeO_{2.73}$ one. This explanation is also in agreement with the fact that the tangent to the data points of molar volume of our Sn-rich samples points at the molar volume of Brownmillerite-type $SrFeO_{2.5}$ in Fig. 2a.

4.2. Lattice and structural properties

Figs. 3a and c show the crystal structures of the orthorhombic end-members $SrSnO_3$ (SG *Pbnm*) [9] and

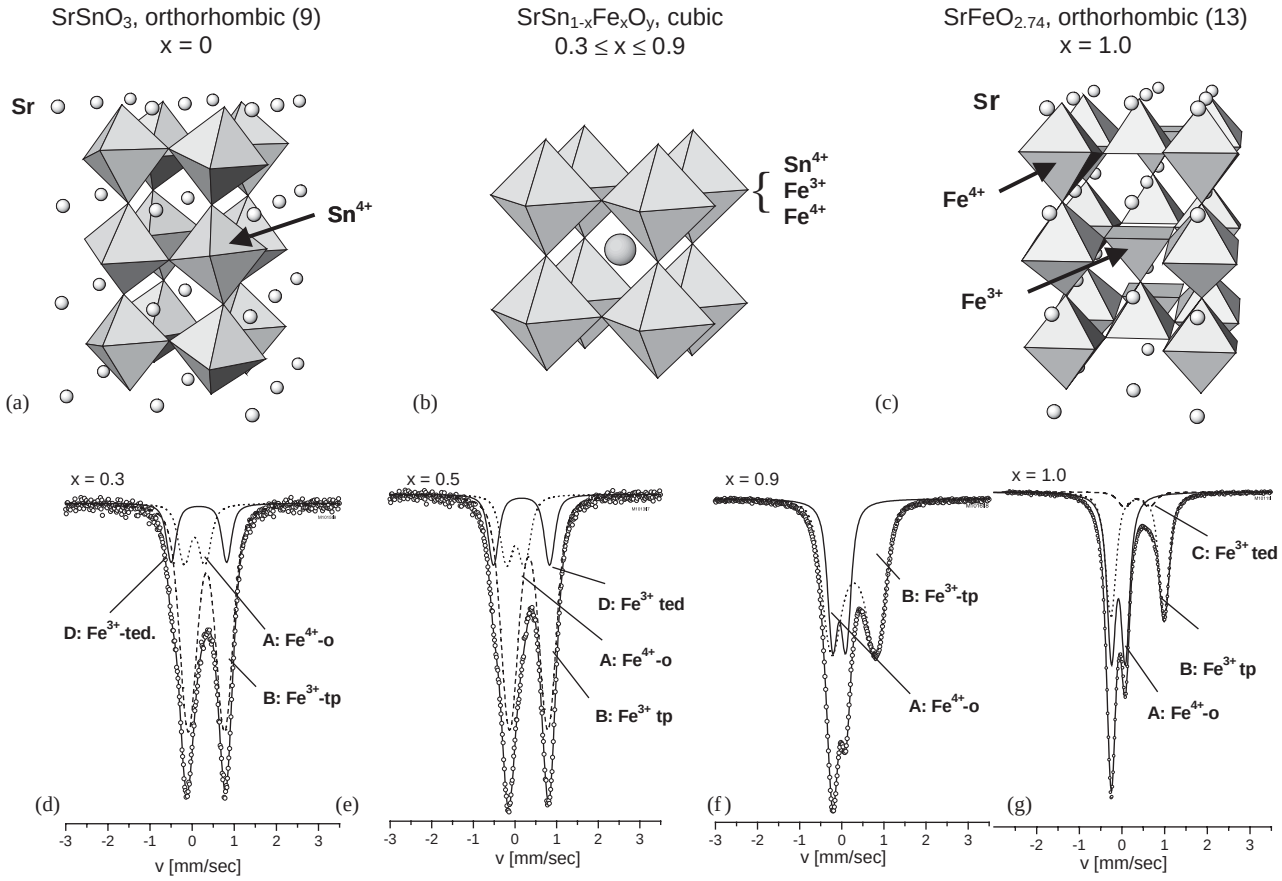

Fig. 3. Structure plots and ^{57}Fe-Mössbauer spectra of members of the $SrSn_{1-x}Fe_xO_y$ solid series (samples were quenched from 620°C).

$SrFeO_{2.74}$ (SG *Cmmm*) [13]. In the structure of $SrSnO_3$, the *B*-positions are occupied by symmetrically equivalent Sn^{4+} ions in tilted octahedral chains. In $SrFeO_{2.74}$, the *B*-positions are split and occupied by ordered Fe^{4+} and Fe^{3+} ions. The tetravalent Fe ions are octahedrally coordinated, whereas the trivalent Fe is in five-fold coordination in form of a tetragonal pyramid. The latter coordination is the result of ordering of oxygen vacancies along the [100]-direction.

As XRPD of Sn rich solid solutions show superstructure reflections (Fig. 1) identical to those of $SrSnO_3$ end-member these compounds are supposed to be isotypic to orthorhombic $SrSnO_3$ [9] with space group *Pbnm* (Fig. 3a). With increasing Fe-content, the superstructure reflections become continuously weaker and disappear between $x = 0.2$ and 0.3 in case of the quenched and between $x = 0.3$ and 0.4 in case of the FC samples. According to the results of the Rietveld refinement the shift of the ions from special positions of the ideal perovskite lattice becomes continuously weaker and less significant (Table 2). Such a behavior can therefore be interpreted in terms of a compositionally driven phase transition from $SrSnO_3$ structure type to cubic perovskite which takes place between $x = 0.2$ and 0.3 in LN samples. The transition point is shifted to $0.3 \leqslant x \leqslant 0.4$ for FC samples, which were annealed down to lower temperatures. As the intermediate solid solutions are found to be of simple cubic perovskite structure Fe and Sn ions are supposed to be disordered over the *B*-positions. Any ordering of these ions should have been detected by XRPD because of the great difference in the number of electrons (and therefore in scattering factor) of these ions (Fe^{3+}:$N_{El} = 23$; Sn^{4+}:$N_{El} = 46$).

A second phase transition was detected between $x = 0.9$ and end-member $SrFeO_y$. Doping of $SrFeO_y$ with Sn leads to a disordered distribution of these ions which suppresses the ordering of oxygen ions. The latter leads to the orthorhombic distortion of the structure of pure $SrFeO_y$, which is monitored in XRPD by the splitting of the cubic (002)-c peak (Fig. 8d). As in the cubic solid solutions no splitting is observed (Fig. 8a–c) it can be due to no pronounced ordering of vacancies exists in the intermediate part of the system.

Fig. 2 shows the lattice constants vs. composition. Lattice parameters as well as molar volume decrease continuously with increasing iron content. This general decrease is consistent with the smaller ionic radii of

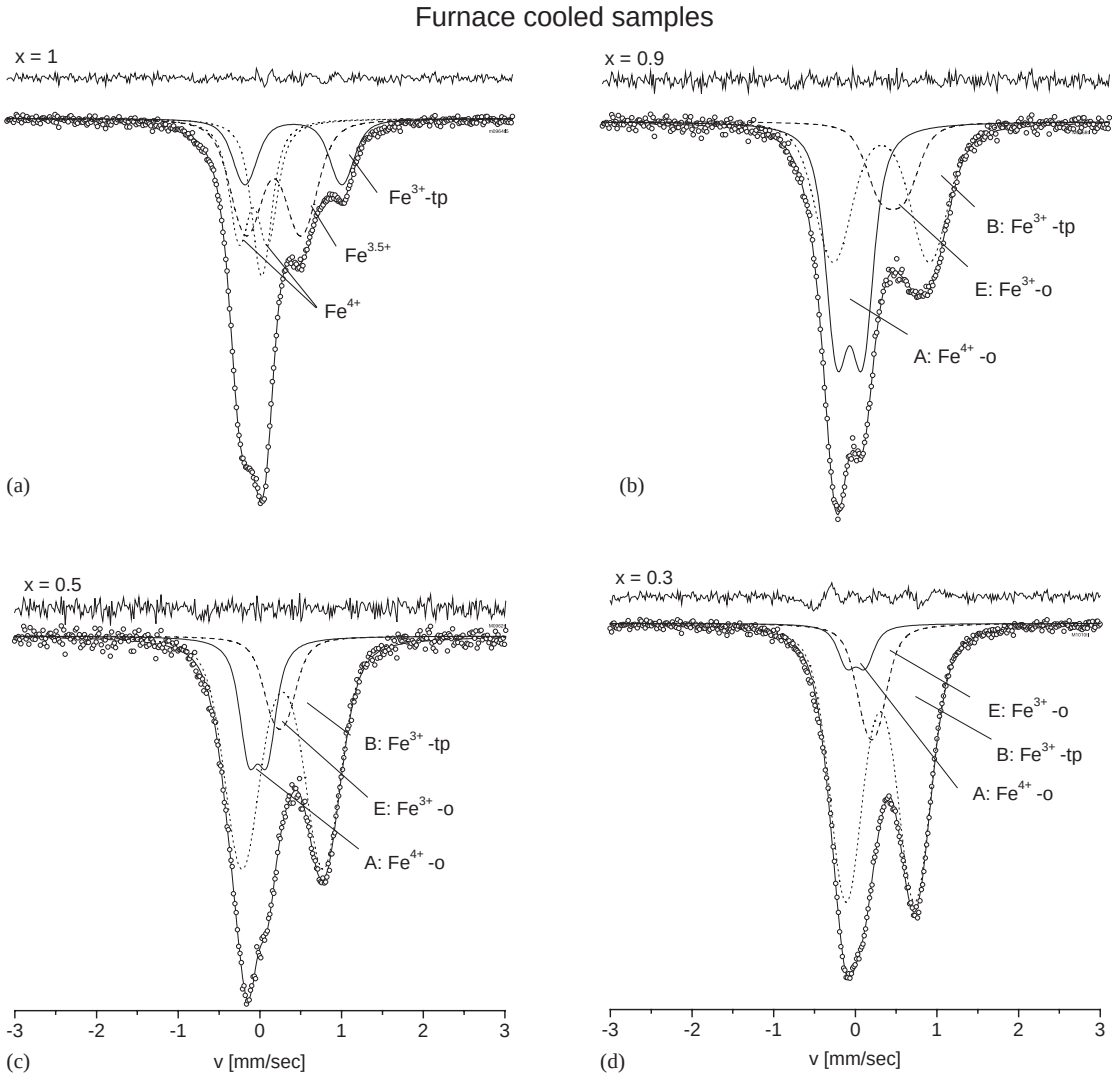

Fig. 4. ^{57}Fe-Mössbauer spectra of members of the $SrSn_{1-x}Fe_xO_y$ solid series. Samples were furnace cooled down to RT.

Fe^{3+} and Fe^{4+} compared with Sn^{4+} for octahedral coordination [18]. No discontinuities could be detected near the two compositionally driven phase transitions at $x \approx 0.35$ and $x \approx 0.95$. Therefore, these transitions are supposed to be of second order.

The non-linearity of molar volume can be explained by a significant amount of $SrFeO_{2.5}$ component superior to a non-ideal behavior of the volumetric properties of the system (Fig. 2a). Generally, a non-linear behavior of the molar volume is explained by means of non-ideality of thermodynamic properties (here the volumetric properties) of solid solutions. But this explanation only holds for binary systems. As mentioned in Section 4.1 with decreasing Fe content a third component, $SrFeO_{2.5}$, appears (Fig. 6) and replaces in part the $SrFeO_{2.73}$ component. As the molar volume $SrFeO_{2.5}$ in Brownmillerite structure-type is greater than that of $SrFeO_{2.73}$ (Fig. 2) it is reasonable to assume that such a replacement enhances the increase of the molar volume of the solid solutions parallel to the increasing $SrSnO_3$-component.

4.3. Valence distribution

Fig. 9 shows a plot of the variation of isomer shift (IS) with quadrupolar splitting (QS) for the $Sr(Sn_{1-x},Fe_x)O_y$ solid solution series (LN) together with data from literature. The regions for the different Mössbauer species like Fe^{3+} in undistorted and distorted octahedral coordination as well as tetrahedral Fe^{3+} and Fe^{4+} l.s. and h.s. (low and high spin) were taken from Wyss et al. [19]. Accordingly, we can distinguish five different regions corresponding to different Fe-species.

I. Fe^{4+} cations in slightly distorted octahedral coordination with a small quadrupole splitting.

Table 3
Quenched samples: ^{57}Fe-Mössbauer parameters at room temperature of the $Sr(Sn_{1-x},Fe_x)O_y$ solid solution series

	Spec	Assignment	IS (mm/s)	QS (mm/s)	σ-QS (mm/s)	Area (%)	y
1.0	A	Fe^{4+}-o	−0.09	0.35	0.07	48	2.74
	B	Fe^{3+}-tp	0.39	1.21	0.13	40	
	C	Fe^{3+}-ted	0.18	0.92	0.41	13	
0.9	A	Fe^{4+}-o	−0.06	0.31	0.14	33	2.70
	B	Fe^{3+}-tp	0.29	0.91	0.37	67	
0.7	A	Fe^{4+}-o	−0.02	0.37	0.18	20	2.72
	B	Fe^{3+}-tp	0.31	0.90	0.38	69	
	C	Fe^{3+}-ted	0.16	1.35	0.17	11	
0.6	A	Fe^{4+}-o	−0.01	0.40	0.20	18	2.75
	B	Fe^{3+}-tp	0.32	0.89	0.35	72	
	C	Fe^{3+}-ted	0.16	1.34	0.15	10	
0.5	A	Fe^{4+}-o	0.01	0.43	0.20	15	2.79
	B	Fe^{3+}-tp	0.33	0.92	0.32	69	
	C	Fe^{3+}-ted	0.16	1.34	0.15	16	
0.4	A	Fe^{4+}-o	0.03	0.48	0.21	15	2.83
	B	Fe^{3+}-tp	0.34	0.91	0.30	73	
	C	Fe^{3+}-ted	0.16	1.34	0.13	12	
0.3	A	Fe^{4+}-o	0.06	0.49	0.19	14	2.87
	B	Fe^{3+}-tp	0.34	0.86	0.31	73	
	C	Fe^{3+}-ted	0.16	1.32	0.12	13	
0.15	A	Fe^{4+}-o	−0.07	—	0.15	5	2.93
	B	Fe^{3+}-tp	0.35	0.68	0.23	59	
	C	Fe^{3+}-ted	0.22	1.16	0.37	37	

Note: IS: isomer shift relative to α-iron; QS: quadrupole splitting; σ-QS: QS-distribution parameter. Coordination of ions: Fe^{4+}-o: octahedral; -tp: tetragonal pyramidal; -ted: tetrahedral.

Table 4
Furnace cooled samples: ^{57}Fe-Mössbauer parameters at room temperature of the $Sr(Sn_{1-x},Fe_x)O_{3-y}$ solid solution series

x	Spec	Assignment	IS (mm/s)	QS (mm/s)	σ-QS (mm/s)	Area (%)	y
1.0[a]		Fe^{3+}-tp	0.40	1.15	0.19	18	2.82
		$Fe^{3.5+}$	0.17	0.65	0.29	38	
		Fe^{4+}-I	0.01	—	0.13	18	
		Fe^{4+}-II	−0.07	0.34	0.13	26	
0.9	A	Fe^{4+}-o	−0.07	0.30	0.16	43	2.74
	B	Fe^{3+}-tp	0.30	1.14	0.34	41	
	E	Fe^{3+}-o	0.44	0.29	0.25	16	
0.7	A	Fe^{4+}-o	0.01	0.26	0.17	24	2.73
	B	Fe^{3+}-tp	0.26	1.02	0.34	66	
	E	Fe^{3+}-o	0.29	0.30	0.18	10	
0.5	A	Fe^{4+}-o	−0.02	0.23	0.12	19	2.80
	B	Fe^{3+}-tp	0.28	0.99	0.33	68	
	E	Fe^{3+}-o	0.24	0.18	0.18	12	
0.3	A	Fe^{4+}-o	0.01	0.23	0.11	7	2.86
	B	Fe^{3+}-tp	0.31	0.85	0.33	78	
	E	Fe^{3+}-o	0.20	0.16	0.17	15	

Note: IS: isomer shift relative to α-iron; QS: quadrupole splitting; σ-QS: QS-distribution. Coordination of ions: Fe^{4+}-o: octahedral; -tp: tetragonal pyramidal. I,II: different Fe^{4+} species according to Ref. [12].

[a] sample was treated as a mixture of $SrFeO_{2.73}$ and $SrFeO_{2.86}$ and fitted using the Mössbauer parameter given by Takeda et al. [12].

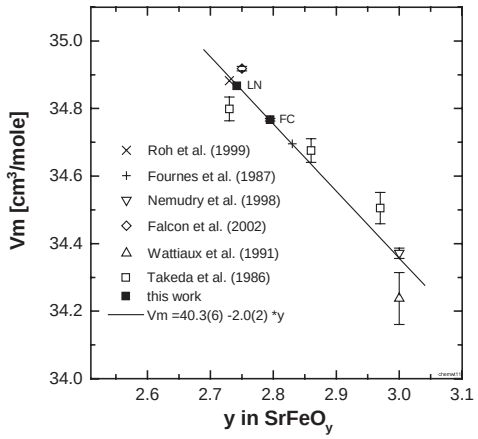

Fig. 5. Plot of molar volume vs. compositional parameter y of the $SrFeO_y$ system. Literature data from [6,12,13,17,24,25].

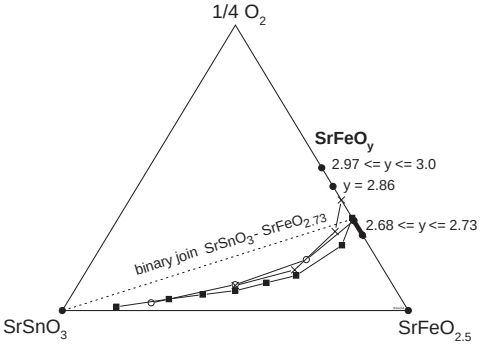

Fig. 6. Location of members of the solid solution series $SrSn_{1-x}Fe_xO_y$ within the phase diagram $SrSnO_3$–$SrFeO_{2.5}$–$1/4O_2$. Open circles: data from Ref. [6]; full squares: this work, quenched samples; crosses: this work, furnace cooled samples. Phases on the join $SrFeO_{2.5}$–$1/4O_2$ according to Ref. [12]. The plot shows the good agreement between our samples and those of Ref. [6] and the fact that all the samples are not binary solid solutions between a $SrSnO_3$ and a $SrFeO_{2.73}$ end-member but contain a $SrFeO_{2.5}$ component.

The lower IS values indicate l.s. Fe^{4+}, the higher ones h.s. Fe^{4+} [20].

II. Fe^{3+} in a distorted tetrahedral coordination with QS ranging up to 1.6 mm/s for tetrahedral Fe^{3+} in $Sr_2Fe_2O_5$.

III. Fe^{3+} ions in an undistorted octahedral coordination.

IV. Fe^{3+} ions in an distorted octahedral coordination with isomer shifts equal to III but with a range of quadrupole splittings comparable to II.

V. Fe^{3+} in fivefold coordination. In contrast to Wyss et al. [19] the Mössbauer parameter for this species were taken from the spectrum of $SrFeO_y$ end-member (Fig. 3g), as this is the single compound containing a well characterized [13] five-fold (tetragonal-pyramidal) coordinated Fe^{3+} site. The representing data point of this species is located within the field, which was attributed to distorted octahedral ferric iron. Therefore, by means of Mössbauer spectroscopy alone it is impossible to distinguish between these two coordinations.

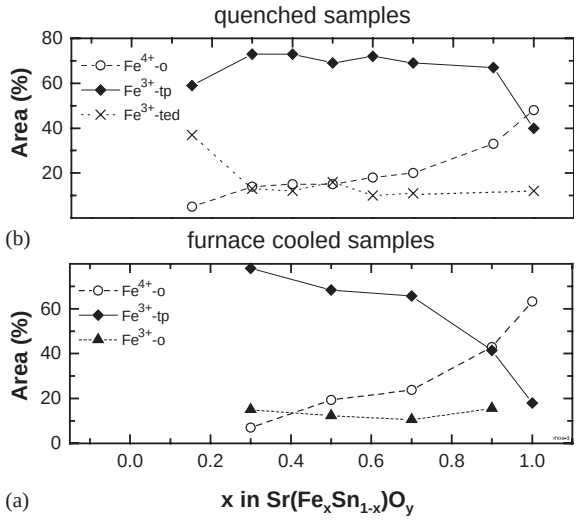

Fig. 7. Area ratios of ^{57}Fe-Mössbauer species of the $SrSn_{1-x}Fe_xO_y$ solid series.

Fig. 9 shows as full squares the representing data points of our quenched samples from Figs. 3d–g. We attribute doublet A to low spin Fe^{4+}-o in octahedral coordination, doublet B to Fe^{3+}-tp in five-fold (tetragonal pyramidal) coordination and dublet C to tetrahedrally coordinated Fe^{3+}-ted.

An initial decrease in QS for Fe^{3+}-tp and an increase in its distribution parameter σ (Figs. 7a and b) was recorded when going from ordered and orthorhombic $SrFeO_{2.74}$ end-member to cubic Sn-containing solid solutions. The increase of σ indicates a broadened distribution of the properties of the chemical environment for this species. XPRD in mind we interpret this as a result of disordered incorporation of Sn onto both Fe^{3+} as Fe^{4+} sites (Fig. 3c) leading to an immediate break down of the structural ordering scheme of $SrFeO_{2.74}$ end-member which is connected with a relaxation of the polyhedra depending on their individual neighborhood.

In contrast to that the QS distribution parameter σ of the tetravalent species is only weakly influenced showing that these ions keep the geometry of their octahedral coordination constant.

According to Fig. 7 in the furnace cooled as well as in the quenched samples the content of Fe^{4+} is strongly reduced from 50% to 60% in the Fe end-member to around 10–15% in tin-rich members with $x = 0.15$. Proportional to that the amount of four- and five-fold

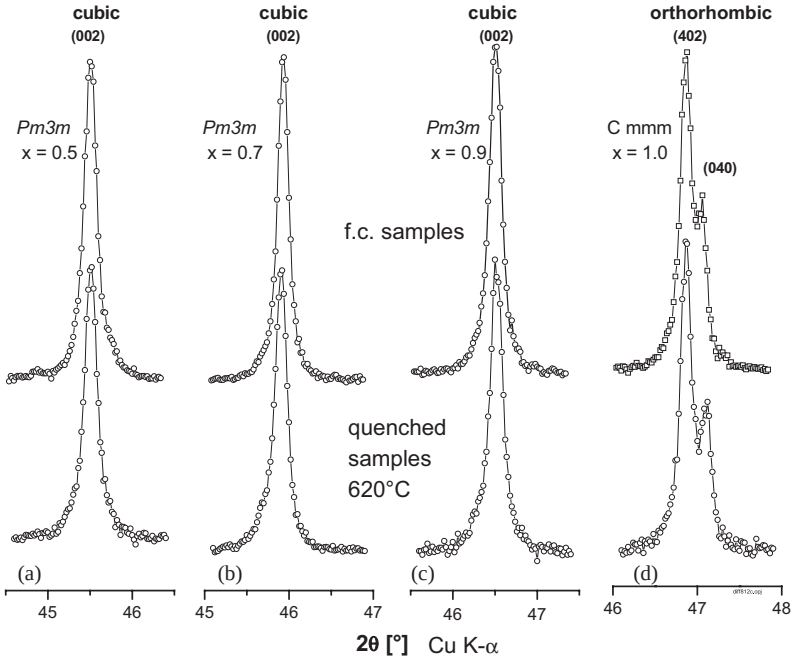

Fig. 8. Development of the simple cubic (002)-c reflection with composition in the iron rich portion of XRPD of members of the $SrSn_{1-x}Fe_xO_y$ solid series.

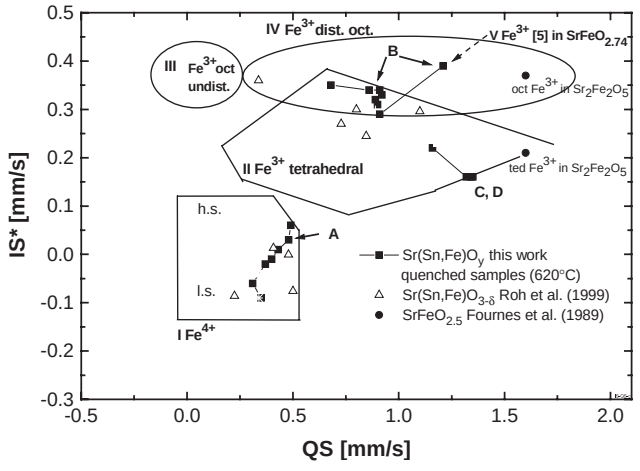

Fig. 9. Variation of isomer shift (IS relative to α-Fe) with quadrupole splitting of the system $SrSn_{1-x}Fe_xO_y$ and reference data for Fe^{3+} and Fe^{4+} in perovskites (regions for Fe-species after Ref. [19]).

coordinated Fe^{3+} species is strongly increased indicating that the vacancies in the oxygen lattice are coupled to the iron ions.

The Mössbauer spectra of the furnace cooled samples show that the Fe end-member $SrFeO_x$ (Fig. 4a) is, according to Takeda et al. [12], a two phase mixture of $SrFeO_{2.74}$ and $SrFeO_{2.86}$. In the spectra of the intermediate solid solutions we have identified a doublet E with a low QS which can be assigned to octahedral Fe^{3+}-o which was not observed in the quenched samples. In contrast to that the quenched samples show a doublet C for tetrahedral Fe^{3+} to which the shoulder on the low-velocity side of the left main absorption peak was due. These differences are supposed to result from the higher degree of oxidation of the furnace cooled samples. This is proved in case of the Fe end-member by Fig. 5 and for the solid solutions by Fig. 10. The latter plot presents the differences in molar volume of quenched and furnace cooled samples $\Delta V_m = V_{LN} - V_{FC}$. The FC-samples have a significantly smaller molar volume which is according to Fig. 5 connected with a higher degree of oxidation. This observation shows that the closing temperature for the uptake of oxygen is well below 620°C. As ΔV_m was found to be proportional to the Fe content we conclude that the Fe^{3+}-ion is the species which is oxidized.

5. Conclusions

In contrast to previous investigations [6] on Sr $(Sn_{1-x}Fe_x)O_y$ perovskite solid solutions we found substantial deviations from simple cubic metric. At room temperature Sr $(Sn_{1-x}Fe_x)O_y$ solid solutions show two compositionally driven phase transitions from orthorhombic $SrSnO_3$ structure to cubic perovskite and from the latter to orthorhombic $SrFeO_{2.74}$ end-member which are supposed to be of second order.

At constant oxygen fugacity and syntheses temperature, the Fe^{4+}/Fe^{tot} ratio was found to be compositionally dependent at (e.g., quenched samples, Fig. 7). Such an effect is already known from the redox pair $Fe^{2+}/$

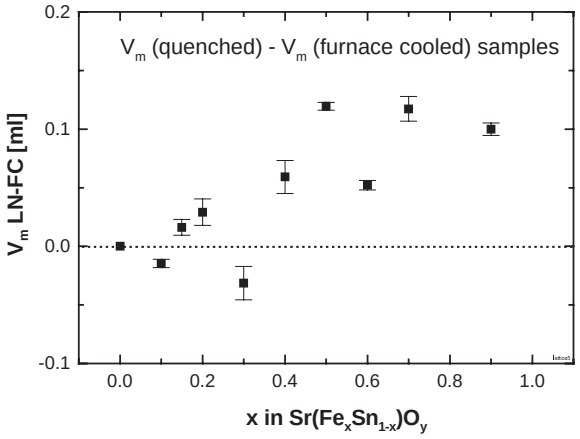

Fig. 10. Differences in molar volume between quenched (620°C) and of furnace cooled samples.

Fe^{3+} in mineral systems (e.g., Fe-bearing synthetic turmalines [21] and lazulites $(Mg,Fe^{2+},Fe^{3+})Al_2(OH)_2(PO_4)_2$ [22]) and could be interpreted in terms of equilibrium thermodynamics.

The curved line of sample compositions of a nominally "binary solid solution" in a ternary system (Fig. 6) is rather uncommon. As our solid solutions (quenched samples) are single phased perovskites it is likely that in the system $SrSnO_3$–$SrFeO_{2.5}$–$SrFeO_{2.73}$ a two-dimensional field, e.g., a ternary solid solution, exists the compositions of which should be adjustable by varying the oxygen fugacity.

Further investigations on this system will deal with the stability of $Sr(Sn_{1-x}Fe_x)O_y$ solid solutions under higher oxygen fugacities, the detailed characterization of lattice symmetry of intermediate compounds and the valence properties of Sn using electron microscopy and ^{119}Sn-Mössbauer spectroscopy.

Acknowledgments

One of us (V.T.) thanks the German Academic Exchange Service (DAAD) and the University of Kiel for the financial support.

References

[1] J.B. Goodenough, W. Gräper, F. Holtzberg, D.L. Huber, R.A. Jefever, J.M. Longo, T.R. McGuire, S. Methfessel, in: K.H. Hellwege, A.M. Hellwege (Eds.), Landolt Börnstein Numerical Data and Functional Relationships in Science and Technology, Springer, Berlin, 1970, pp. 126–314.
[2] F.S. Galasso, Perovskite and High Tc Superconductors, Gordon and Breach Science Publishers, New York, 1990.
[3] C.N.R. Rao, J. Mater. Chem. 9 (1999) 1–14.
[4] A.S. Bhalla, R. Guo, R. Roy, Mater. Res. Innovat. 4 (2000) 3–26.
[5] M.A. Pena, J.L.G. Ferro, Chem. Rev. 101 (2001) 1981–2017.
[6] K.S. Roh, K.H. Ryu, C.H. Yo, J. Solid State Chem. 142 (1999) 288–293.
[7] V. Thangadurai, P. Schmid Beurmann, W. Weppner, Mater. Res. Bull. 37 (2002) 599–604.
[8] V. Thangadurai, P. Schmid Beurmann, W. Weppner, Mater. Sci. Eng. B, in press.
[9] A. Vegas, M. Vallet-Regí, J.M. Gonzáles-Calbet, M.A. Alario-Franco, Acta Crystallogr. B 42 (1986) 167–172.
[10] ICDD 22-1442, Natl. Bur. Stand. (US) Monograph 25 8 80, 1970.
[11] J. Mizusaki, M. Okaysu, S. Yamauchi, K. Fueki, J. Solid State Chem. 99 (1992) 166–172.
[12] Y. Takeda, K. Kanno, T. Takada, O. Yamamoto, M. Takano, N. Nakayama, Y. Bando, J. Solid State Chem. 63 (1986) 237–249.
[13] H. Falcon, J.A. Barbero, J.A. Alonso, M.J. Martínez-Lope, J.L.G. Fierro, Chem. Mater. 14 (5) (2002) 2325–2333.
[14] C.L. Lengauer, HILL, Institut für Mineralogie, Kristallographie und Strukturchemie der Universität Wien, 1993.
[15] D.G. Rancourt, A.M. MacDonald, A.E. Lalonde, J.Y. Ping, Am. Mineral. 78 (1993) 1–7.
[16] D.G. Rancourt, J.Y. Ping, Nucl. Instr. Meth. Phys. Res. B 58 (1991) 85–97.
[17] L. Fournés, Y. Potin, J.C. Grenier, G. Demazeau, M. Pouchard, Solid State Commun. 62 (4) (1987) 239–244.
[18] R.D. Shannon, Acta Crystallogr. A 32 (1976) 751–767.
[19] M. Wyss, A. Reller, H.R. Oswald, Solid State Ionics 101–103 (1997) 547–554.
[20] M. Takano, T. Okita, N. Nakayama, Y. Bando, Y. Takeda, O. Yamamoto, J.B. Goodenough, J. Solid State Chem. 73 (1988) 140–150.
[21] B. Velickov, I. Abs-Wurmbach, Eur. J. Mineral. 12Bh (2000) 221.
[22] R. Selke, P. Schmid-Beurmann, L. Cemič, Eur. J. Mineral., 2003, accepted for publication.
[23] L. Fournés, Y. Potin, J.C. Grenier, P. Hagenmuller, Rev. Phys. Appl. 24 (1989) 463–468.
[24] A. Wattiaux, L. Fournés, A. Demargues, N. Bernaben, J.C. Grenier, M. Pouchard, Solid State Commun. 77 (7) (1991) 489–493.
[25] A. Nemudry, M. Weiss, I. Gainutdinov, V. Boldyrev, R. Schöllhorn, Chem. Mater. 10 (1998) 2403–2411.